Growth of lanthanide-doped LiGdF$_4$ nanoparticles induced by LiLuF$_4$ core as tri-modal imaging bioprobes

Xuesong Zhai [a, 1], Pengpeng Lei [a, b, 1], Peng Zhang [c], Zhuo Wang [a, b], Shuyan Song [a], Xia Xu [a], Xiuling Liu [a], Jing Feng [a, *], Hongjie Zhang [a, *]

[a] State Key Laboratory of Rare Earth Resource Utilization, Changchun Institute of Applied Chemistry, Chinese Academy of Sciences, 5625 Renmin Street, Changchun 130022, China
[b] University of Chinese Academy of Sciences, Beijing 100049, China
[c] Department of Radiology, The Second Hospital of Jilin University, Changchun 130041, China

ABSTRACT

Multimodal imaging can compensate for the deficiencies and incorporate the advantages of individual imaging modalities. In this paper, we demonstrated the synthesis of core–shell nanocomposites LiLuF$_4$@LiGdF$_4$:Yb,Er/Tm constituted of tetragonal LiLuF$_4$ nanoparticles as core and Yb,Er/Tm-codoped LiGdF$_4$ as shell. LiLuF$_4$@LiGdF$_4$:Yb,Er/Tm nanoparticles display brighter upconversion luminescence (UCL) than NaGdF$_4$:Yb,Er/Tm nanoparticles with the same size under continuous-wave excitation at 980 nm. The active shell layer of LiGdF$_4$:Yb,Er/Tm not only provide the UCL center, but also serve as magnetic resonance (MR) imaging contrast agent. To further improve the UCL intensity, the inert LiGdF$_4$ shell was coated on the LiLuF$_4$@LiGdF$_4$:Yb,Er/Tm nanoparticles. Furthermore, LiLuF$_4$@LiGdF$_4$:Yb,Tm@LiGdF$_4$ nanoparticles have been successfully applied to UCL/X-ray computed tomography (CT)/MR tri-modal imaging on the modal of tumor-bearing mice.

© 2015 Elsevier Ltd. All rights reserved.

1. Introduction

Lanthanide (Ln^{3+})-doped upconversion nanoparticles (UCNPs), which can convert near-infrared (NIR) radiation into NIR or visible or ultraviolet (UV) light, are receiving a great deal of attention for potential application in bioimaging and photodynamic therapy (PDT) [1–6]. The UCNPs have many advantages over conventional biomarkers, such as deep penetration of NIR excitation light into biological tissue, low toxicity, and high signal-to-noise ratio as well as high resistance to photobleaching, blinking, and reduced photodamage [7–14]. To date, Ln^{3+}-doped fluorides have been extensively investigated and proved to be the ideal host candidates for producing high upconversion luminescence efficiency [11,13].

Although photoluminescence imaging based on UCNPs is suitable for multiscale imaging from cellular level to whole-body animals, it has one shortcoming of the low penetration depth of less than several centimeters [15–17]. Due to the intrinsic restrictions of every imaging modality, single-modality imaging could not provide enough information for the accurate diagnosis. For more accurate imaging and diagnosis, multimodal imaging probes combining different imaging modalities have been developed. Magnetic resonance imaging (MRI) is widely used to discriminate the infinitesimal change in soft tissues [18–20], and X-ray computed tomography (CT) displays a high degree of spatial resolution of the hard-tissues (<50 μm) [21–23]. All lanthanide elements (from lanthanum to lutetium) have potential X-ray attenuation properties owing to the large atomic number and high X-ray absorption coefficient [24,25]. Gadolinium ions (Gd^{3+}) possess seven unpaired electrons which can efficiently alter the relaxation time of surrounding water protons, and have been widely used in MRI diagnosis of routine clinical disease [26]. Up to now, the studies on the corresponding fluoride UCNPs are mostly focused on BaGdF$_5$ [27,28], GdF$_3$ [29–31], NaGdF$_4$ [32–35], and KGdF$_4$ [36,37] hosts, and few attention has been paid to LiGdF$_4$ host matrix. As known, LiREF$_4$ (RE = Y, Er–Lu) host material is an outstanding host matrix for both upconversion (UC) and down-conversion (DC) luminescence [38–42]. Mahalingam et al. reported that their synthesized Yb and Tm codoped LiYF$_4$ UCNPs not only exhibit intense UC emission under excitation at 980 nm, but also generate additional emission lines in the deep-UV (294 nm) and near-infrared regions

---

(1.46 μm), which can be used for anti-counterfeiting and telecommunication applications, respectively [38]. Huang et al. reported that the total upconversion quantum yield of $LiLuF_4$:Yb,Tm/Er core–shell nanoparticles was almost 5 times higher than that of $NaYF_4$:Yb,Tm/Er core–shell nanoparticles which, for a long time, was considered to be one of the most efficient host lattices [41]. They also found an enhanced efficacy of $LiYF_4$:Yb,Er UCNPs-based PDT agent for the inhibition of tumor growth both in vitro and in vivo due to high energy transfer efficiency [42]. Although $LiREF_4$ (RE = Y, Er–Lu) UCNPs have been widely reported, a systematic survey on the optical and magnetic properties of $LiGdF_4$ nanoparticles is still lacking because the syntheses of tetragonal-phase $LiGdF_4$ UCNPs via wet chemical method is challenging [31,43,44] and instead, orthorhombic-phase GdF_3 is apt to be formed (Fig. S1).

Herein, our strategy is based on using small $LiLuF_4$ core to induce the growth of tetragonal-phase $LiGdF_4$ shells. $LiLuF_4$@$LiGdF_4$:Yb,Er/Tm nanoparticles show intense UCL than β-$NaGdF_4$:Yb,Er/Tm UCNPs. We also constructed the optically inert $LiGdF_4$ shell layer around $LiLuF_4$@$LiGdF_4$:Yb,Er/Tm nanoparticles to enhance the UCL intensity. Furthermore, the feasibility of $LiLuF_4$@$LiGdF_4$:Yb,Tm@$LiGdF_4$ core-shell-shell nanoparticles to be applied as UCL/CT/T_1-weighted MR tri-modal imaging bioprobes was investigated.

2. Materials and methods

2.1. Chemicals and materials

$LnCl_3$ (Ln = Lu, Gd, Yb, Er, and Tm, 99.99%) compounds were purchased from Shanghai Shabo Chemical Technology Company. Oleic acid (OA) and 1-octadecene (ODE) were obtained from Alfa Aesar. Trifluoroacetic lithium (CF_3COOLi) was purchased from Aladdin. Ammonium fluoride (NH_4F) and lithium hydroxide (LiOH) with the purity of A.R. was bought from Beijing Fine Chemical Company, China.

2.2. Synthesis of tri-modal imaging probes

2.2.1. Synthesis of $LiLuF_4$ or GdF_3 nanoparticles

The typical procedure is as follows: 1 mmol of $LnCl_3$ (Ln = Lu or Gd) was added to a 100 mL four-necked flask containing 10 mL of OA and 10 mL of ODE. The solution was stirred and heated to 110 °C for 1 h under vacuum and then cooled to room temperature (RT) with the gentle flow of Ar gas. A solution of 4 mmol of NH_4F and 2.5 mmol of LiOH in 10 mL of methanol was added, and then the solution was kept at 50 °C for 30 min. After methanol was evaporated, the reaction was then heated to 310 °C rapidly under Ar atmosphere, kept for 1 h and then cooled to RT. The nanoparticles were precipitated with ethanol, collected by centrifugation, and redispersed in cyclohexane.

2.2.2. Synthesis of $LiLuF_4$@$LiGdF_4$:Yb,Er/Tm core–shell nanoparticles

The shell stock solution was obtained by mixing 1 mmol of $LnCl_3$ (Ln = Gd, Yb, and Er or Tm) in a 100 mL four-necked flask containing 10 mL of OA and 10 mL of ODE. The solution was stirred and heated to 110 °C for 1 h under vacuum and then cooled to RT with the gentle flow of Ar gas. The as-prepared $LiLuF_4$ core and 2.5 mmol of CF_3COOLi in cyclohexane were then mixed together into the above solution. The mixture solution was degassed at 120 °C for 30 min under Ar flow to remove the remaining water, cyclohexane and oxygen. Then, the resulting mixture was heated to 305 °C rapidly under Ar flow with stirring for 1 h. Then, the solution was cooled down to RT. The solid products were precipitated by addition of ethanol, collected by centrifugation, and redispersed in cyclohexane.

2.2.3. Synthesis of $LiLuF_4$@$LiGdF_4$:Yb,Er/Tm@$LiGdF_4$ core-shell-shell nanoparticles

The synthesis procedures for shell coating of $LiGdF_4$ on $LiLuF_4$@$LiGdF_4$:Yb,Er/Tm nanoparticles were similar to those for shell coating of $LiGdF_4$:Yb,Tm/Er on $LiLuF_4$ nanoparticles except that 1 mmol $GdCl_3$ was used to prepare the shell stock solution. The prepared $LiLuF_4$@$LiGdF_4$:Yb,Er/Tm@$LiGdF_4$ nanoparticles were dispersed in cyclohexane.

2.2.4. Surface modification of OA-capped UCNPs

Water-soluble UCNPs were prepared according to the reported method [16]. The as-prepared oleic acid-capped nanoparticles in cyclohexane solution were dispersed in 10 mL HCl solution (pH = 2) and ultrasonicated for 15 min to remove the surface ligands. After the reaction, the nanoparticles were collected via centrifugation at 10,000 rpm for 15 min, and further purified by adding acidic ethanol solution. The resulting products were washed with ethanol and deionized water for several times, redispersed in 20 mg/mL sodium citrate solution, and washed with deionized water for three times.

2.3. Characterization

The phase identification was performed by X-ray diffraction (XRD) (Model Rigaku Ru-200b), using a nickel-filtered Cu Kα radiation (λ = 1.5406 Å) in the range of $10° \leq 2\theta \leq 70°$. Transmission electron microscopy (TEM), high-resolution TEM (HRTEM) imaging, and electron diffraction pattern were implemented by a JEM-2100F electron microscope at 200 kV. FT-IR spectra were recorded on a BioRad Fourier transform infrared spectrometer with the KBr method. Under the excitation at 980 nm, UCL spectra were recorded using a SPEX1000M spectrometer (1.5 mm for slit width). The temporal properties were studied by using a 953.6 nm Raman shifter pulsed laser with a pulse width of 10 ns and a repetition rate of 10 Hz, a monochromator, and a digital oscilloscope. All the measurements were performed at RT.

2.4. Cytotoxicity assay

The in vitro cytotoxicity of the core-shell-shell nanoparticles was tested by using the typical methyl thiazolyl tetrazolium (MTT) reduction assay on Hela cells. Hela cells were cultivated in a 96-well cell-culture plate at a density of 10^4 per well at 37 °C under 5% CO_2 for 24 h. Successively, different concentrations of $LiLuF_4$@$LiGdF_4$:Yb,Tm@$LiGdF_4$ (0, 15.6, 31.25, 62.5, 125, 250, 500, 1000 μg/mL, diluted in RPMI 1640 culture medium) were added to the wells. After incubation for 24 h, 20 μL of MTT solution (5 mg/mL) was added to each well and the plate was incubated for an additional 4 h. After formation of formazan dye, the medium was removed from the wells. Then, the formazan dye was extracted into DMSO. The optical density at 490 nm (OD_{490}) of each well was measured on a microplate reader. The cell viability could be calculated by the following formula: Cell viability (%) = (mean of absorbance value of treatment group/mean of absorbance value of control) × 100%.

2.5. Animal experiments

Animal care and handing procedures were in agreement with the guidelines of the Regional Ethics Committee for Animal Experiments. The H22 cells were cultured and injected subcutaneously in the left axilla of each Balb/c mouse. The mice were used for experiments when the tumors had grown to reach the size of

~200 mm^3.

2.6. In vivo UCL imaging

The tumor-bearing mouse was anesthetized (with 10% chloral hydrate) and intratumorally injected with LiLuF$_4$@LiGdF$_4$:Yb,Tm@LiGdF$_4$ nanoparticles. Then, the mouse was imaged on an *in vivo* Maestro (CRi) imaging system. An external 980 nm laser is assembled to the imaging system as the excitation source.

2.7. In vitro and in vivo X-ray CT imaging

For *in vitro* CT imaging, to assess CT contrast efficacy, sodium citrate capped LiLuF$_4$@LiGdF$_4$:Yb,Tm@LiGdF$_4$ nanoparticles and iobitridol (commercial CT contrast agent, 350 mg I/mL) were dispersed in deionized water with different (Lu+Yb+Gd) and I concentrations.

For *in vivo* CT imaging, firstly, the tumor-bearing mouse was anesthetized and scanned to get the CT image before injection of the contrast agent. Successively, the tumor-bearing mouse was intratumorally injected of sodium citrate capped LiLuF$_4$@LiGdF$_4$:Yb,Tm@LiGdF$_4$ nanoparticles (50 μL, 20 mg/mL) and scanned. To study the biodistribution of the UCNPs, 200 μL of UCNPs (70 mg/mL) was intravenously injected to a mouse. Then, the mouse was scanned at time intervals. *In vitro* and *in vivo* CT images were collected using a Philips 256-slice CT scanner. Imaging parameters were as follows: thickness, 0.9 mm; pitch, 0.99; 120 kVp, 300 mA; field of view, 350 mm; gantry rotation time, 0.5 s; table speed, 158.9 mm s^{-1}.

2.8. In vitro and in vivo T$_1$ weighted MR imaging

For *in vitro* MR imaging, sodium citrate capped LiLuF$_4$@LiGdF$_4$:Yb,Tm@LiGdF$_4$ nanoparticles were dispersed in water at different Gd concentrations ranging from 0 to 25 mM. The longitudinal relaxivity values (r_1) were acquired on a Huantong 1.5 T MR scanner.

For *in vivo* MR imaging, the tumor-bearing mouse was anesthetized and intratumorally injected of sodium citrate capped LiLuF$_4$@LiGdF$_4$:Yb,Tm@LiGdF$_4$ nanoparticles (50 μL, 15 mM). The T_1-weighted images of before and after intratumoral injection were acquired using 1.5 T human clinical scanner (Siemens Medical System).

3. Results and discussion

3.1. Synthesis and characterization

The crystal phase of the synthesized nanoparticles was determined by the XRD patterns. All synthesized nanoparticles show well-defined diffraction peaks, confirming their good crystallinity (Fig. 1). Usually, LiREF$_4$ crystal has a tetragonal structure (space group $I4_1/a$) with single site symmetry of S_4 for all RE^{3+} ions [41]. As shown in Fig. 1a, the XRD pattern of the core nanoparticles agrees well with the standard pattern of tetragonal-phase LiLuF$_4$ (JCPDS No. 027-1251). Er^{3+}-doped UCNPs show the same XRD pattern with Tm^{3+}-doped UCNPs. Fig. 1b and c shows the XRD patterns of LiLuF$_4$@LiGdF$_4$:Yb,Er and LiLuF$_4$@LiGdF$_4$:Yb,Er@LiGdF$_4$ nanoparticles. Their XRD patterns can be indexed to pure tetragonal-phase LiGdF$_4$, and no trace of other phases or impurities were detected. In addition, compared with the diffraction peaks of pure LiLuF$_4$ nanocrystals, the shifting of X-ray diffraction (XRD) peaks towards the low-angle side indicates that the average size of the crystal unit cell expanded slightly after treatment of the core–shell
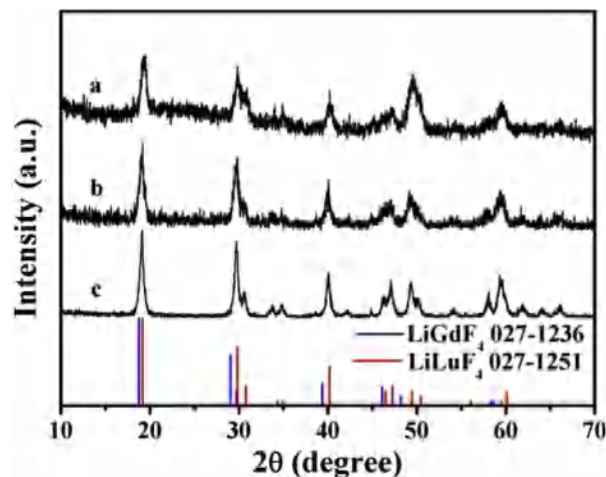

Fig. 1. XRD patterns of LiLuF$_4$ core-only (a), LiLuF$_4$@LiGdF$_4$:Yb,Er core–shell (b), and LiLuF$_4$@LiGdF$_4$:Yb,Er@LiGdF$_4$ core-shell-shell nanoparticles (c).

structure with Gd substituted matrix (Fig. S2), justified by the fact that Gd^{3+} is larger in ionic size than the previous occupant Lu^{3+}. The average particle size of the products can be estimated from the Scherrer formula, D = $K\lambda/\beta cos\ \theta$, where D is the average particle size, λ is the X-ray wavelength (0.15405 nm), β is the full-width at half-maximum, θ is the diffraction angle of an observed peak, and K is a constant (0.89), respectively [44]. The average nanoparticle sizes were calculated to be 13, 17, and 21 nm for core-only, cor-e–shell and core-shell-shell nanoparticles, respectively, which basically agree with that estimated from the TEM results (Fig. 2). Er^{3+}-doped UCNPs show the same morphology and particle size with Tm^{3+}-doped UCNPs counterparts. Fig. 2 shows the TEM images of the synthesized LiLuF$_4$ core-only, LiLuF$_4$@LiGdF$_4$:Yb,Er cor-e–shell and LiLuF$_4$@LiGdF$_4$:Yb,Er@LiGdF$_4$ core-shell-shell nanoparticles as the examples. As one can see in Fig. 2a, the as-synthesized LiLuF$_4$ core-only nanoparticles were roughly rhomboid and monodisperse, with an average length of ~12.5 nm. Compositional analysis by energy dispersive X-ray analysis (EDXA) revealed the existence of Lu^{3+} and F$^-$ ions in LiLuF$_4$ core-only nanoparticles (Fig. S3). From Fig. 2b and c, it can be seen that the particle sizes of core–shell and core-shell-shell structured nanoparticles increase obviously, while their morphology and monodispersity are well maintained after being coated with LiGdF$_4$ shell. Histograms of the size distribution of the core-only, core–shell, and core-shell-shell nanoparticles are shown in Fig. S4. Based on the difference in particle sizes between the core-only, core–shell, and core-shell-shell nanoparticles, the shell thickness was estimated to be around 2.5 nm and 4.5 nm for the core–shell and core-shell-shell nanoparticles, respectively. No aggregation was observed in the as-prepared nanoparticles, which is attributable to the presence of the long-chain oleic acid on the crystal surface. The cor-e–shell nanostructures were also confirmed by the change in EDXA results. As shown in Fig. S3, the EDXA indicates the presence of Gd and Yb elements in LiLuF$_4$@LiGdF$_4$:Yb,Er nanoparticles. The selected area electron diffraction (SAED) patterns of core-only, core–shell, and core-shell-shell nanoparticles are presented. As shown in Fig. 2d–f, their SAED display a similar diffraction pattern, which can be indexed to the tetragonal-phase LiLuF$_4$ and LiGdF$_4$ structures. The clear lattice fringes across the single particle in HRTEM image show good crystallinity of the as-prepared nanoparticles, which also benefitted UCL emission (inset of Fig. 2a–c). The interplanar spacing of 0.46 nm and 0.47 nm also corresponded well to the d-spacing of the (110) facets of the tetragonal phase
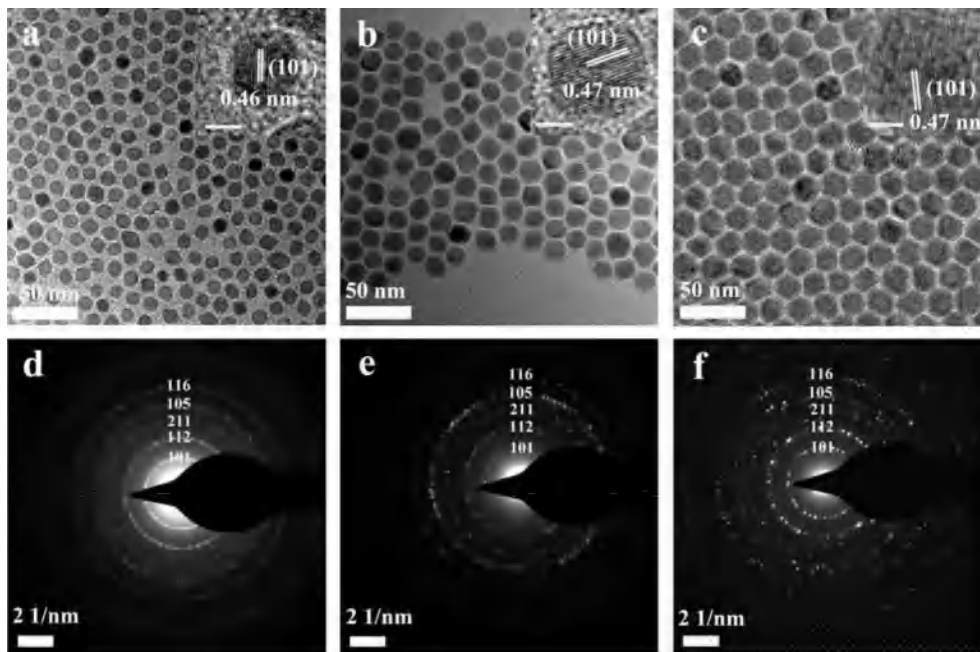
Fig. 2. TEM images and SAED patterns of LiLuF$_4$ core-only (a, d), LiLuF$_4$@LiGdF$_4$:Yb,Er core–shell (b, e), LiLuF$_4$@LiGdF$_4$:Yb,Er@LiGdF$_4$ core-shell-shell nanoparticles (c, f). The insets are the corresponding HRTEM images for (a), (b), and (c).

LiLuF$_4$ and LiGdF$_4$, respectively. All above analyses demonstrate that the LiLuF$_4$ core can induce the growth of tetragonal-phase LiGdF$_4$ shell through constructing the core–shell structure.

To achieve multicolor UC emissions, LiGdF$_4$ nanoparticles doped with different activators were synthesized. The UCL spectra of the samples feature the distinct emission bands of Er^{3+} and Tm^{3+}, respectively. As shown in Fig. 3a, blue UC emissions (in the web version) from LiLuF$_4$@LiGdF$_4$:Yb,Tm nanoparticles dispersed in cyclohexane (1 wt %) can be observed by the naked eye. Three visible emissions were observed to be centered at 452, 475, 650 nm assigned to the $^1D_2 \rightarrow {}^3F_4$, $^1G_4 \rightarrow {}^3H_6$, and $^1G_4 \rightarrow {}^3F_4$ transitions of Tm^{3+} ion, respectively. Furthermore, an intensive NIR emission from $^3H_4 \rightarrow {}^3H_6$ transition was detected as well and its intensity was very strong and more than 3 times higher than that of all other UCL bands, which is beneficial for *in vivo* imaging. LiLuF$_4$@LiGdF$_4$:Yb,Er nanoparticles yield a green emission, whose spectra show the red emission of $^4F_{9/2} \rightarrow {}^4I_{15/2}$ (~658 nm), and relatively stronger green emissions of $^2H_{11/2} \rightarrow {}^4I_{15/2}$ (~525 nm), $^4S_{3/2} \rightarrow {}^4I_{15/2}$ (~544 nm) transitions, respectively. The spectra of LiLuF$_4$@LiGdF$_4$:Yb,Er nanoparticles show more distinct Stark splitting than those of GdF$_3$:Yb,Er nanoparticles at room temperature (Fig. S5), which indicate that they possess different crystal structures. To evaluate if LiGdF$_4$ is an efficient UCL host, the UCL properties of nanoparticles were compared with those of 18 nm sized NaGdF$_4$:Yb,Er/Tm nanoparticles (Fig. S6). In order to allow for accurate comparison, we used the same doping levels of Ln^{3+} ions for these two types of LiGdF$_4$ and NaGdF$_4$ nanoparticles that are capped by the same ligand of oleic acid. NaGdF$_4$ was selected for this comparison since NaGdF$_4$ host material was an efficient UCL host matrix and demonstrated as useful T_1 MRI contrast agent (CA). As shown in Fig. S7a, the UCL intensities of LiLuF$_4$@LiGdF$_4$:Yb,Er nanoparticles, e.g. green UCL at 521/543 nm and red UCL at 650 nm, are about 1.7 and 1.3 times higher than that of NaGdF$_4$:Yb,Er nanoparticles, while the blue emission of LiLuF$_4$@LiGdF$_4$:Yb,Tm nanoparticles at 450/476 nm, the red emission at 650 nm, and the NIR UCL is at 800 nm are 2.1, 3.7, and 1.6 times higher than the ones of nanoparticles NaGdF$_4$:Yb,Tm nanoparticles (Fig. S7). The results indicate that LiGdF$_4$ is also a promising UCL host material.

Generally, for Ln^{3+}-doped nanoparticles with small size, their surface area-to-volume ratio is very high and a large portion of the dopants should be located at the surface [45,46]. Thus, the excitation energy will then be easily quenched by the surface defects, impurities and vibrational deactivation from solvents or surface-bound ligands. As a consequence, the UCL intensity of Ln^{3+}-doped LiGdF$_4$ is severely limited by surface-related quenching. To further improve the UCL efficiency, a useful strategy to address this problem is to construct a core–shell structure, in which the epitaxial shell not only isolate lanthanide dopants from the environment but also can passivate surface lattice defects. The UCL of core–shell and core-shell-shell nanoparticles dispersed in hexane were compared and shown in Fig. 3. The UCL intensities of LiLuF$_4$@LiGdF$_4$:Yb,Tm@LiGdF$_4$ and LiLuF$_4$@LiGdF$_4$:Yb,Er@LiGdF$_4$ core-shell-shell nanoparticles are about 11 and 7.5 times higher than those of their core–shell counterparts. Moreover, to further substantiate the influence of shell on the optical properties of Ln^{3+}-doped LiGdF$_4$ nanoparticles, the fluorescence dynamic curves of Tm^{3+} and Er^{3+} were also measured, respectively. By fitting the fluorescence dynamic curves with the double exponential function, the rise and decay time are lengthened remarkably after coating the inert shell (Fig. 3c and d). For example, the rise time was increase from 0.067 and 0.034 ms in core–shell nanocrystals to 0.149 and 0.058 ms in core-shell-shell counterparts, while the corresponding decay time was found to increase from 0.188 and 0.091 ms in core–shell nanocrystals to 0.425 and 0.156 ms in core-shell-shell counterparts, respectively. The observed stronger UCL intensity and longer UCL lifetime (decay or rise time) of core-shell-shell nanoparticles are due to the core-shell-shell structure that effectively separates in space the surface quenchers from the UC emitters. As such, multiphonon relaxation processes of the Tm^{3+} and Er^{3+} ions mediated by high vibrational energies of the surface organic ligands and surface defects can be reduced, which thus enhance the generation of UCL.

In order to understand the UCL process in these Ln^{3+}-doped UCNPs, power dependence studies were performed on various UC emission channels. Generally, the output UC emission intensity (I) is proportional to the pump power (P) via the following formula,
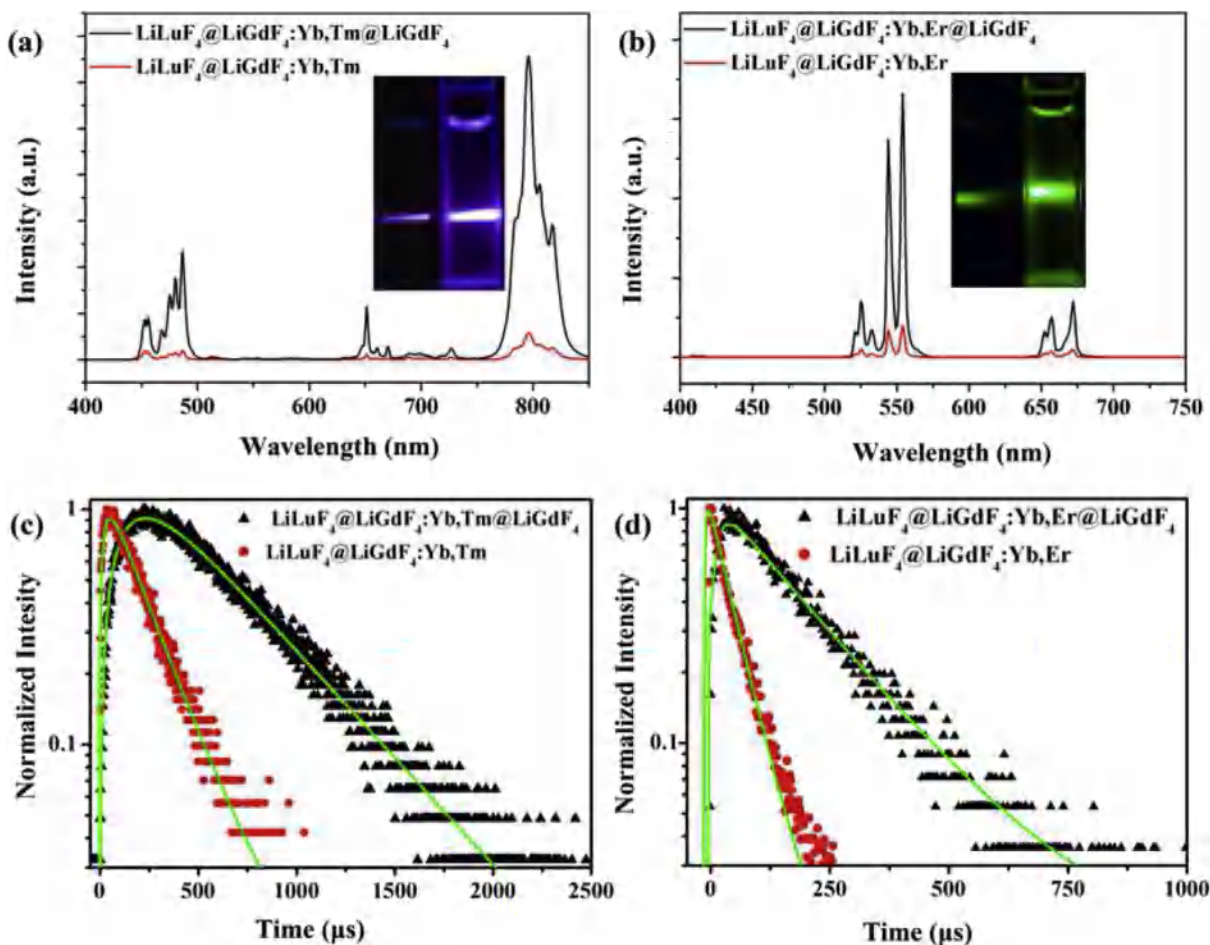
Fig. 3. UCL spectra (a, b) and fluorescence dynamic curves (c, d) (monitoring the Tm^{3+} and Er^{3+} emissions at 800 nm and 650 nm, respectively) of $LiLuF_4$@$LiGdF_4$:Yb,Tm/Er@$LiGdF_4$ and $LiLuF_4$@$LiGdF_4$:Yb,Tm/Er UCNPs.

$I \propto P^n$, where n is the number of pump photons required to populate the upper emitting level. Therefore, the slope of the luminescence intensity versus pump power in the double-logarithmic coordinate will indicate the photon number absorbed in each UCL process [13,14]. Upon excitation at 980 nm, for LiLu-F_4@$LiGdF_4$:Yb,Tm nanoparticles, the slopes for the $^1D_2 \rightarrow {}^3F_4$, $^1G_4 \rightarrow {}^3H_6$ and $^3H_4 \rightarrow {}^3H_6$ transitions of Tm^{3+} were determined to be 3.81, 2.65, 1.69, respectively (Fig. S8a), which infers that the UC
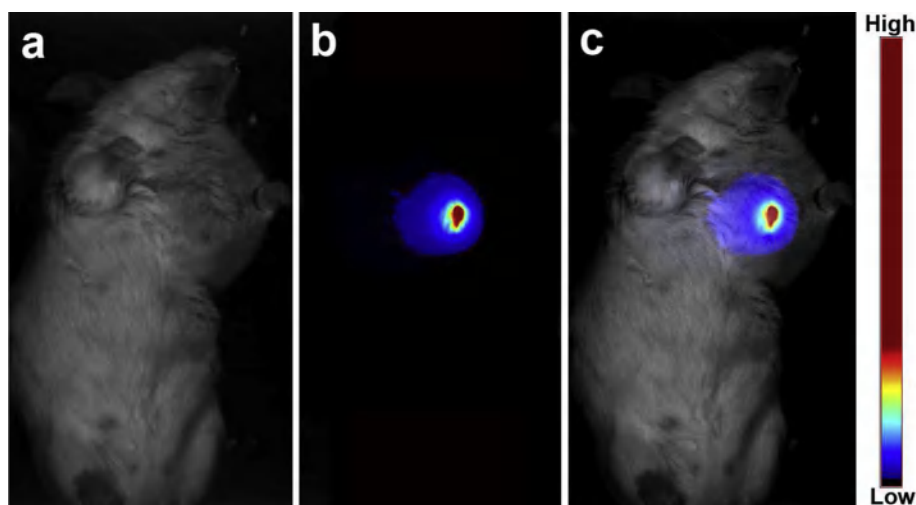

Fig. 4. *In vivo* UCL imaging of a tumor-bearing mouse after injection of $LiLuF_4$@$LiGdF_4$:Yb,Tm@$LiGdF_4$ nanoparticles at the tumor site: bright field (a), upconversion luminescence (b), and overlay images (c).
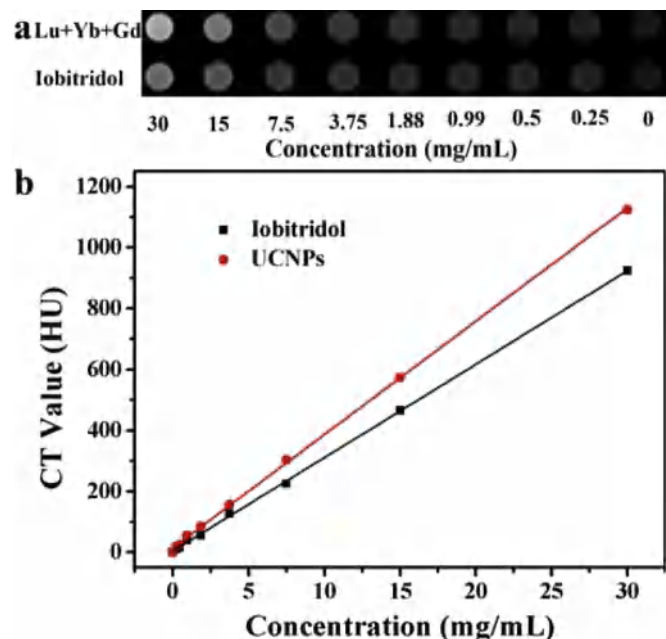
Fig. 5. *In vitro* CT images of LiLuF$_4$@LiGdF$_4$:Yb,Tm@LiGdF$_4$ nanoparticles and iobitridol at different concentrations (a) and CT value (HU) of UCNPs and iobitridol as a function of the concentrations of Ln^{3+} ions (Lu, Yb and Gd) and I, respectively (b).

emissions from $^1D_2$ and $^1G_4$ to $^3H_6$ were realized through multiphoton process (n = 4 or 3) while the UC emission from $^3H_4$ to $^3H_6$ was achieved via two-photon process. For LiLuF$_4$@LiGdF$_4$:Yb,Er nanoparticles, the slope values of $^4S_{3/2} \rightarrow {}^4I_{15/2}$ and $^4F_{9/2} \rightarrow {}^4I_{15/2}$ were fitted to be 2.02 and 1.88, respectively (Fig. S8b). Hence, both the UC emissions from $^2H_{11/2}$ ($^4S_{3/2}$) and $^4F_{9/2}$ to $^4I_{15/2}$ occurred via two-photon process as shown by the energy level diagrams for the UCL process of Er^{3+}.

The hydrophobic oleic acid capped LiLuF$_4$@LiGdF$_4$:Yb,Tm/Er@LiGdF$_4$ nanoparticles were transferred into aqueous phase with sodium citrate for further biological evaluation and imaging applications. The successful ligand exchange reaction was further verified by FT-IR and TGA curves (Fig. S9).

3.2. In vitro cytotoxicity

The cytotoxicity of the hydrophilic UCNPs was investigated to evaluate the potential for further *in vivo* imaging applications. The cytotoxicity of the hydrophilic UCNPs against HeLa cells was evaluated when the cells were exposed to 0–1000 μg/mL for 24 h with a standard MTT assay. As shown in Fig. S10, the HeLa cell viability (102%) was not hindered by the UCNPs up to 1000 μg/mL after 24 h treatment. The result demonstrates low cytotoxicity and good biocompatibility of the modified hydrophilic UCNPs.

3.3. In vivo upconversion luminescence (UCL) imaging

UCL imaging is an important imaging procedure in diagnostic medicine due to the high sensitivity and photostability. To demonstrate the capacity of Ln^{3+}-doped UCNPs for small animal UCL imaging *in vivo*, we injected LiLuF$_4$@LiGdF$_4$:Yb,Tm@LiGdF$_4$ core-shell-shell nanoparticles with intense 800 nm NIR emission (as shown in Fig. 3a) into the tumor site of the mouse. The NIR input (980 nm) and output (800 nm) UCL signal are benefit for UCL imaging due to the deep tissue penetration. It is can be seen from Fig. 4 that the strong NIR UCL signal could be detected from the tumor site by the *in vivo* Maestro (CRi) imaging system. The overlay image confirmed that the high contrast between the background and the UCL signal. It indicated that LiLuF$_4$@LiGdF$_4$:Yb,Tm@LiGdF$_4$ core-shell-shell nanoparticles have great potential as the bioprobe in UCL imaging.

3.4. In vitro and in vivo X-ray CT imaging

X-ray CT imaging is one of the most popular clinical diagnosis tools because of the deep penetration of tissues and organs. Lanthanide elements possess intrinsic advantages for X-ray imaging owing to the larger X-ray absorption efficiency. As known, the higher the atomic number and electron density is, the higher the attenuation coefficient is. Therefore, we choose LiLuF$_4$ as core to induce growth of LiGdF$_4$ shell and it could be expected that core-shell-shell nanoparticles have the good imaging ability in X-ray CT imaging. To assess the X-ray imaging effect of LiLuF$_4$@LiGdF$_4$:Yb,Tm@LiGdF$_4$, different concentrations of the core-shell-shell nanoparticles were monitored by X-ray CT to
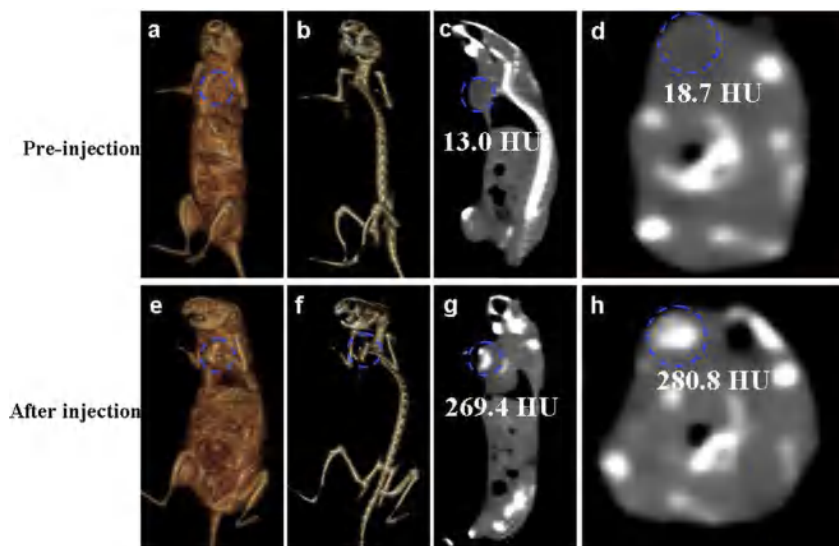

Fig. 6. *In vivo* CT images of a tumor-bearing mouse before (a–d) and after (e–h) injection of LiLuF$_4$@LiGdF$_4$:Yb,Tm@LiGdF$_4$ nanoparticles at the tumor site. The position of tumor was marked by blue circles. (For interpretation of the references to colour in this figure legend, the reader is referred to the web version of this article.)
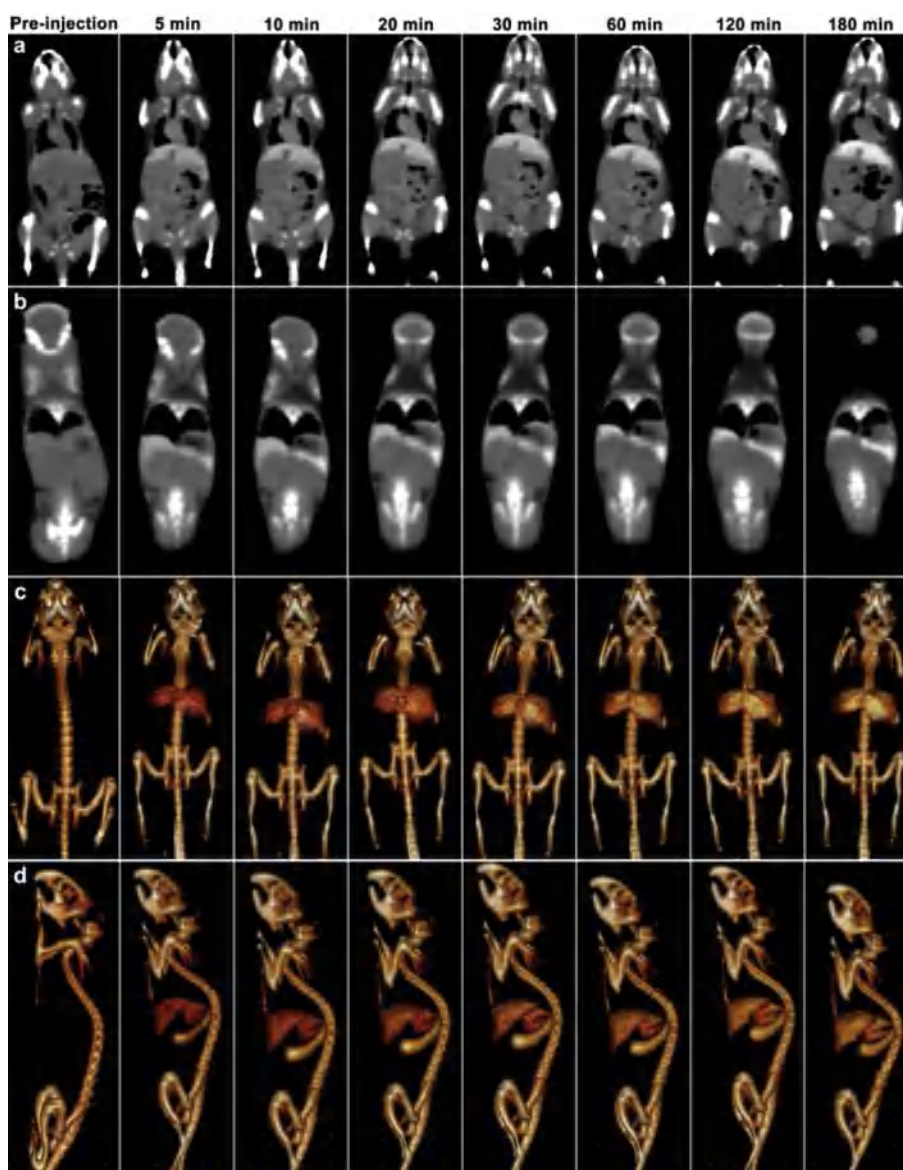
Fig. 7. *In vivo* CT imaging. Coronal view images of mouse after intravenous injection of LiLuF$_4$@LiGdF$_4$:Yb,Tm@LiGdF$_4$ (200 μL, 50 mg/mL) solution at timed intervals. Heart and liver (a). Spleen and kidney (b). The corresponding 3D renderings of *in vivo* CT images (c, d).

determine the Hounsfield units (HU) value, using iobitridol as the standard (Fig. 5a and b). A good linear correlation between the HU value and the concentration of Ln (Ln = Gd, Lu, and Yb) or I was observed. Nevertheless, at equivalent concentrations, the X-ray absorption of LiLuF$_4$@LiGdF$_4$:Yb,Tm@LiGdF$_4$ nanoparticles was higher than that of iobitridol, indicating the good X-ray CT imaging ability of UCNPs and its potential as a CT imaging agent.

For *in vivo* CT imaging, we first injected a solution of the core-shell-shell nanoparticles intratumorally. A clear contrast enhancement could be detected from the tumor site after injection (Fig. 6). Also, we detected the HU values of the tumor site after injection of the core-shell-shell nanoparticles. The HU values were different at the different positions. For coronal position, the value is 269.4 HU. For transversal position, the value is a little higher as 280.8 HU. Furthermore, the time-dependent of the UCNPs distribution in the mouse was tracked by CT imaging after intravenous injection. At timed intervals, the evident enhancement of the signals in different organs could be seen. An enhancement of the signal of the heart could be observed after 5 min. The liver and spleen imagings were greatly enhanced from 5 min to 3 h. (Fig. 7). A more careful look at

the 3D-renderings of CT images showed evident enhancement of the signals of liver and spleen within this same period of time as well. This long-lasting liver-signal enhancement may improve the detection of the hepatic metastases. The results demonstrated that the UCNPs have the feasibility to be served as an *in vivo* CT contrast agent.

3.5. In vitro and in vivo MR imaging (MRI)

Gd-containing nanoparticles could accelerate longitudinal relaxivity of water protons and improve the quality of MR images, especially the soft tissues imaging. To explore the potential of using LiLuF$_4$@LiGdF$_4$:Yb,Tm@LiGdF$_4$ nanoparticles as T_1-weighted MRI contrast agents, *in vitro* and *in vivo* MRI measurements are carried out. Fig. 8a shows a series of T_1-weighted MR images with different Gd^{3+} concentration. As the Gd^{3+} concentration increase, the UCNPs brightened the MR images, which suggest that the nanoparticles could act as T_1-weighted MRI contrast agents. The longitudinal relaxivity value is determined to be 0.7922 mM^{-1} s^{-1} according to the slope of T_1 relaxation rates ($1/T_1$) and Gd concentrations

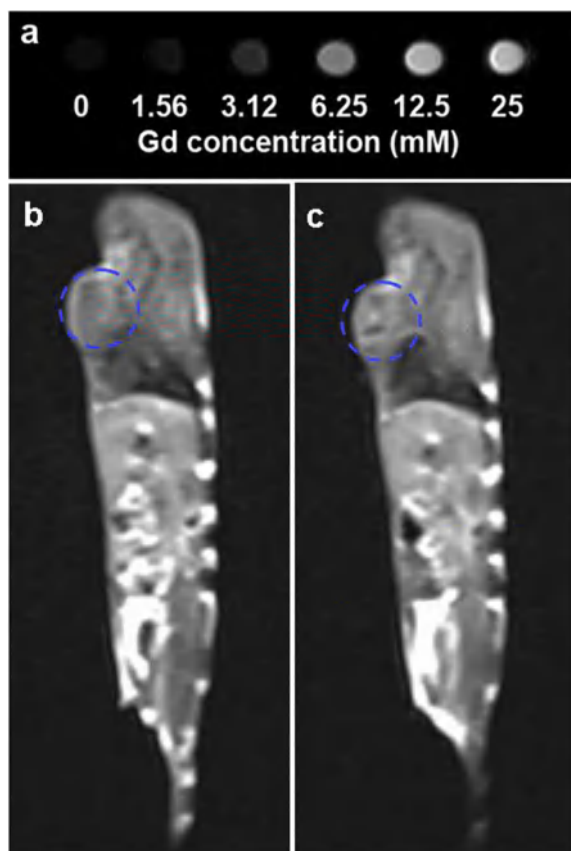**Fig. 8.** *In vitro* T_1-weighted MR images of LiLuF$_4$@LiGdF$_4$:Yb,Tm@LiGdF$_4$ at different Gd concentrations (a). *In vivo* T_1-weighted MR images of tumor-bearing mouse at pre-injection (b), and after injection of sodium citrate modified UCNPs (c) in situ. The position of tumor was marked by blue circles. (For interpretation of the references to colour in this figure legend, the reader is referred to the web version of this article.)

(Fig. S11). Furthermore, the application of *in vivo* MR imaging for tumor-bearing mouse was also examined after intratumoral injection of the UCNPs. Compared with pre-contrast T_1-weighted MR image, the post-contrast T_1-weighted MR image showed significant contrast enhancement in the tumor site of the mouse (Fig. 8b and c). The *in vivo* MR images indicate the UCNPs could be good T_1-weighted MRI contrast agents for biomedical applications.

4. Conclusions

In summary, the growth of lanthanide-doped LiGdF$_4$ shell induced by LiLuF$_4$ core has been achieved successfully via a simple high boiling solvent process. Such LiLuF$_4$@LiGdF$_4$:Yb,Er/Tm nanoparticles display bright upconversion luminescence, reflecting that the LiGdF$_4$ is an excellent host for upconversion luminescence. The UCL intensity is improved significantly after coating the LiGdF$_4$ shell. Using LiLuF$_4$@LiGdF$_4$:Yb,Tm@LiGdF$_4$ nanoparticles as a UCL probe, high contrast UCL imaging of the tumor-bearing mouse was achieved. Importantly, the *in vitro* and *in vivo* CT and MR imaging studies confirm that the UCNPs could be applied as the contrast agent for CT and MR imaging. The results make LiLuF$_4$@LiGdF$_4$:Yb,Tm@LiGdF$_4$ nanoparticles the candidate for UCL/CT/MR tri-modal imaging bioprobes.

Acknowledgments

Appendix A. Supplementary data

Supplementary data related to this article can be found at http://dx.doi.org/10.1016/j.biomaterials.2015.06.023.

References

[1] J. Zhou, Z. Liu, F. Li, Upconversion nanophosphors for small-animal imaging, Chem. Soc. Rev. 41 (2012) 1323—1349.
[2] F. Wang, X.G. Liu, Recent advances in the chemistry of lanthanide-doped upconversion nanocrystals, Chem. Soc. Rev. 38 (2009) 976—989.
[3] C. Wang, L. Cheng, Z. Liu, Drug delivery with upconversion nanoparticles for multi-functional targeted cancer cell imaging and therapy, Biomaterials 32 (2011) 1110—1120.
[4] G. Tian, W.Y. Yin, J.J. Jin, X. Zhang, G.M. Xing, S.J. Li, et al., Engineered design of theranostic upconversion nanoparticles for tri-modal upconversion luminescence/magnetic resonance/X-ray computed tomography imaging and targeted delivery of combined anticancer drugs, J. Mater. Chem. B 2 (2013) 1378—1389.
[5] D.M. Yang, Y.L. Dai, J.H. Liu, Y. Zhou, Y.Y. Chen, C.X. Li, et al., Ultra-small BaGdF$_5$-based upconversion nanoparticles as drug carriers and multimodal imaging probes, Biomaterials 35 (2014) 2011—2023.
[6] Q. Chen, C. Wang, L. Cheng, W.W. He, Z.P. Cheng, Z. Liu, Protein modified upconversion nanoparticles for imaging-guided combined photothermal and photodynamic therapy, Biomaterials 35 (2014) 2915—2923.
[7] F. Wang, Y. Han, C.S. Lim, Y.H. Lu, J. Wang, J. Xu, et al., Simultaneous phase and size control of upconversion nanocrystals through lanthanide doping, Nature 463 (2010) 1061—1065.
[8] F. Wang, R.R. Deng, J. Wang, Q.X. Wang, Y. Han, H.M. Zhu, et al., Tuning upconversion through energy migration in core-shell nanoparticles, Nat. Mater. 10 (2011) 968—973.
[9] D.E. Achatz, R.J. Meier, L.H. Fischer, O.S. Wolfbeis, Luminescent sensing of oxygen using a quenchable probe and upconverting nanoparticles, Angew. Chem. Int. Ed. 50 (2011) 260—263.
[10] S.W. Wu, G. Han, D.J. Milliron, S. Aloni, V. Altoe, D.V. Talapin, et al., Non-blinking and photostable upconverted luminescence from single lanthanide-doped nanocrystals, Proc. Natl. Acad. Sci. U. S. A. 106 (2009) 10917—10921.
[11] T. Yang, Y. Sun, Q. Liu, W. Feng, P. Yang, F. Li, Cubic sub-20 nm NaLuF$_4$-based upconversion nanophosphors for high-contrast bioimaging in different animal species, Biomaterials 33 (2012) 3733—3742.
[12] J. Wang, R.R. Deng, M.A. MacDonald, B.L. Chen, J.K. Yuan, F. Wang, et al., Enhancing multiphoton upconversion through energy clustering at sublattice level, Nat. Mater. 13 (2014) 157—162.
[13] X.S. Zhai, S.S. Liu, Y.L. Zhang, Q.S. Qin, W.P. Qin, Controlled synthesis of ultrasmall hexagonal NaTm$_{0.02}$Lu$_{0.98-x}$Yb$_x$F$_4$ nanocrystals with enhanced upconversion luminescence, J. Mater. Chem. C 2 (2014) 2037—2044.
[14] M. Pang, X.S. Zhai, J. Feng, S.Y. Song, R.P. Deng, Z. Wang, et al., One-step synthesis of water-soluble hexagonal NaScF$_4$:Yb/Er nanocrystals with intense red emission, Dalton Trans. 43 (2014) 10202—10207.
[15] A. Louie, Multimodality imaging probes: design and challenges, Chem. Rev. 110 (2010) 3146—3195.
[16] Y. Sun, Xingjun Zhu, J.J. Peng, F.Y. Li, Core-shell lanthanide upconversion nanophosphors as four-modal probes for tumor angiogenesis imaging, ACS Nano 7 (2014) 11290—11300.
[17] F. Zhang, Q.H. Shi, Y.C. Zhang, Y.F. Shi, K.L. Kunlun Ding, D.Y. Zhao, et al., Fluorescence upconversion microbarcodes for multiplexed biological detection: nucleic acid encoding, Adv. Mater. 23 (2011) 3775—3779.
[18] X.J. Zhu, J. Zhou, M. Chen, M. Shi, W. Feng, F.Y. Li, Core-shell Fe$_3$O$_4$@NaLuF$_4$:Yb,Er/Tm nanostructure for MRI, CT and upconversion luminescence tri-modality imaging, Biomaterials 33 (2012) 4618—4627.
[19] N.J.J. Johnson, W. Oakden, G.J. Stanisz, R. Scott Prosser, F.C.J.M. van Veggel, Size-tunable, ultrasmall NaGdF$_4$ nanoparticles: insights into their T1 MRI contrast enhancement, Chem. Mater. 23 (2011) 3714—3722.
[20] D.L. Ni, J.W. Zhang, W.B. Bu, H.Y. Xing, F. Han, Q.F. Xiao, et al., Dual-targeting upconversion nanoprobes across the blood-brain barrier for magnetic resonance/fluorescence imaging of intracranial glioblastoma, ACS Nano 8 (2014) 1231—1242.
[21] Y. Liu, K. Ai, L. Lu, Nanoparticulate X-ray computed tomography contrast agents: from design validation to in vivo applications, Acc. Chem. Res. 45 (2012) 1817—1827.
[22] Y.L. Liu, K.L. Ai, J.H. Liu, Q.H. Yuan, Y.Y. He, L.H. Lu, Hybrid BaYbF$_5$ nanoparticles: novel binary contrast agent for high-resolution in vivo X-ray computed tomography angiography, Adv. Healthc. Mater. 1 (2012) 461—466.
[23] Z. Liu, E.G. Ju, J.H. Liu, Y.D. Du, Z.Q. Li, Q.H. Yuan, et al., Direct visualization of gastrointestinal tract with lanthanide-doped BaYbF$_5$ upconversion nanoprobes, Biomaterials 34 (2013) 7444—7452.
[24] Y. Liu, K. Ai, J. Liu, Q. Yuan, Y. He, L.A. Lu, High-performance ytterbium-based

nanoparticulate contrast agent for in vivo X-ray computed tomography imaging, Angew. Chem. Int. Ed. 51 (2012) 1437—1442.

[25] J.B. Ma, P. Huang, M. He, L.Y. Pan, Z.J. Zhou, L.L. Feng, et al., Folic acid-conjugated LaF$_3$:Yb,Tm@SiO$_2$ nanoprobes for targeting dual-modality imaging of upconversion luminescence and X-ray computed tomography, J. Phys. Chem. B 116 (2012) 14062—14070.

[26] P. Caravan, J.J. Ellison, T.J. McMurry, R.B. Lauffer, Gadolinium(III) chelates as MRI contrast agents: structure, dynamics, and applications, Chem. Rev. 99 (1999) 2293—2352.

[27] L.N. Guo, Y.Z. Wang, Y.H. Wang, J. Zhang, P.Y. Dong, Crystal structure and up-and down-conversion properties of Yb^{3+},Ho^{3+} codoped BaGdF$_5$ solid-solution with different morphologies, CrystEngComm. 14 (2012) 3131—3141.

[28] D.M. Yang, Y.L. Dai, J.H. Liu, Y. Zhou, Y.Y. Chen, C.X. Li, et al., Ultra-small BaGdF$_5$-based upconversion nanoparticles as drug carriers and multimodal imaging probes, Biomaterials 35 (2014) 2011—2023.

[29] T. Passuello, M. Pedroni, F. Piccinelli, S. Polizzi, P. Marzola, S. Tambalo, et al., PEG-capped, lanthanide doped GdF$_3$ nanoparticles: luminescent and T2 contrast agents for optical and MRI multimodal imaging, Nanoscale 4 (2012) 7682—7689.

[30] Q. Ju, Y.S. Liu, D.T. Tu, H.M. Zhu, R.F. Li, X.Y. Chen, Lanthanide-doped multi-color GdF$_3$ nanocrystals for time-resolved photoluminescent biodetection, Chem. Eur. J. 17 (2011) 8549—8554.

[31] W.Y. Yin, L.N. Zhao, L.J. Zhou, Z.J. Gu, X.X. Liu, G. Tian, et al., Enhanced red emission from GdF$_3$:Yb^{3+},Er^{3+} upconversion nanocrystals by Li$^+$ doping and their application for bioimaging, Chem. Eur. J. 18 (2012) 9239—9245.

[32] M.Y. Guo, C.Y. Liu, Z.Y. Gao, J.F. Zeng, Y. Hou, F. Fang, et al., Magnetic/upconversion fluorescent NaGdF$_4$:Yb,Er nanoparticle based dual-modal molecular probes for imaging tiny tumors in vivo, ACS Nano 7 (2013) 7227—7240.

[33] J. Ryu, H.Y. Park, K.H. Kim, H.Y. Kim, J.H. Yoo, M. Kang, et al., Facile synthesis of ultrasmall and hexagonal NaGdF$_4$:Yb^{3+},Er^{3+} nanoparticles with magnetic and upconversion imaging properties, J. Phys. Chem. C 114 (2010) 21077—21082.

[34] G.Z. Ren, S.J. Zeng, J.H. Hao, Tunable multicolor upconversion emissions and paramagnetic property of monodispersed bifunctional lanthanide-doped NaGdF$_4$ nanorods, J. Phys. Chem. C 115 (2011) 20141—20147.

[35] M. He, P. Huang, C.L. Zhang, H.Y. Hu, C.C. Bao, G. Gao, et al., Dual phase-controlled synthesis of uniform lanthanide doped NaGdF$_4$ upconversion nanocrystals via an OA/ionic liquid two-phase system for in vivo dual-modality imaging, Adv. Funct. Mater. 21 (2011) 4470—4477.

[36] Q. Ju, D.T. Tu, Y.S. Liu, R.F. Li, H.M. Zhu, J.C. Chen, et al., Amine-functionalized lanthanide-doped KGdF$_4$ nanocrystals as potential optical/magnetic multi-modal bioprobes, J. Am. Chem. Soc. 134 (2011) 1323—1330.

[37] H.T. Wong, F. Vetrone, R. Naccache, H.L.W. Chan, J.H. Hao, J.A. Capobianco, Water dispersible ultra-small multifunctional KGdF$_4$:Tm^{3+},Yb^{3+} nanoparticles with near-infrared to near-infrared upconversion, J. Mater. Chem. 21 (2011) 16589—16596.

[38] V. Mahalingam, F. Vetrone, R. Naccache, A. Speghini, J.A. Capobianco, Colloidal Tm^{3+}/Yb^{3+}-doped LiYF$_4$ nanocrystals: multiple luminescence spanning the UV to NIR regions via low-energy excitation, Adv. Mater. 21 (2009) 4025—4028.

[39] Y.P. Du, Y.W. Zhang, L.D. Sun, C.H. Yan, Optically active uniform potassium and lithium rare earth fluoride nanocrystals derived from metal trifluroacetate precursors, Dalton Trans. 40 (2009) 8574—8581.

[40] G.Y. Chen, T.Y. Ohulchanskyy, A. Kachynski, H. Agren, P.N. Prasad, Intense visible and near-infrared upconversion photoluminescence in colloidal LiYF$_4$: Er^{3+} nanocrystals under excitation at 1490 nm, ACS Nano 5 (2011) 4981—4986.

[41] P. Huang, W. Zheng, S.Y. Zhou, D.T. Tu, Z. Chen, H.M. Zhu, Lanthanide-doped LiLuF$_4$ upconversion nanoprobes for the detection of disease biomarkers, Angew. Chem. Int. Ed. 53 (2014) 1252—1257.

[42] M. Wang, Z. Chen, W. Zheng, H.M. Zhu, S. Lu, E. Ma, et al., Lanthanide-doped upconversion nanoparticles electrostatically coupled with photosensitizers for near-infrared-triggered photodynamic therapy, Nanoscale 6 (2014) 8274—8282.

[43] H. Na, J. Seok, H.J. Chang, Y. Kim, K. Woo, K. Lim, et al., Facile synthesis of intense green light emitting LiGdF$_4$:Yb,Er-based upconversion bipyramidal nanocrystals and their polymer composites, Nanoscle 6 (2014) 7461—7468.

[44] D.M. Yang, G.G. Li, X.J. kang, Z.Y. Cheng, P.A. Ma, C. Peng, et al., Room temperature synthesis of hydrophilic Ln^{3+}-doped KGdF$_4$ (Ln, Ce, Eu, Tb, Dy) nanoparticles with controllable size: energy transfer, size-dependent and color-tunable luminescence properties, Nanoscale 4 (2012) 3450—3459.

[45] X.M. Li, D.K. Shen, J.P. Yang, C. Yao, R.C. Che, F. Zhang, et al., Successive layer-by-layer strategy for multi-shell epitaxial growth: shell thickness and doping position dependence in upconverting optical properties, Chem. Mater. 25 (2013) 106—112.

[46] F. Vetrone, R. Naccache, V. Mahalingam, C.G. Morgan, J.A. Capobianco, The active-core/active-shell approach: a strategy to enhance the upconversion luminescence in lanthanide-doped nanoparticles, Adv. Funct. Mater. 19 (2009) 2924—2929.